

An Experimental Investigation on Rotor-to-Rotor Interactions of Small UAV

Wenwu Zhou¹, Zhe Ning², Haixing Li³, Hui Hu⁴(✉)

Department of Aerospace Engineering, Iowa State University, Ames, Iowa, 50011

In the present study, an experimental investigation was performed to study the effects of rotor-to-rotor interactions on the **aerodynamic and aeroacoustic** performances of small UAVs. It was found that, while the thrust coefficients of rotor were independent of the separation distance, the thrust fluctuations were found to increase dramatically as the separation distance decreased. An enhancement of $\sim 250\%$ was confirmed for the twin-rotor case (i.e., $L = 0.05D$) in comparison with that of the single rotor case, which is believed to be caused by the complex flow interactions within rotors as revealed by the detailed PIV and Stereoscopic PIV measurements. Reducing the separation distance not only intensified the force fluctuations, but also increased the aeroacoustic noise level of the baseline case. Comparing to the $L = 1.0D$ case, a maximum enhancement of ~ 3 dB in aeroacoustic noise was recorded for the $L = 0.05D$ case, which is caused by the severely thrust fluctuations and turbulent flow interactions within rotors.

Nomenclature

BPF	Blade passing frequency $BPF = n * \text{Blade number}$
C_T	Thrust coefficient $C_T = \frac{4T}{\rho n^2 D^4 \pi^3}$
D	Rotor diameter
L	Separation distance
$N. TKE$	$0.5(\overline{u'^2} + \overline{v'^2} + \overline{w'^2}) / U_{tip}^2$
$N. in-plane TKE$	$0.5(\overline{u'^2} + \overline{v'^2}) / U_{tip}^2$
n	Rotor rotation speed
T	Thrust
U_{tip}	Rotor tip speed, $U_{tip} = \omega D / 2$
SPL	Sound pressure level
β	Azimuthal angle
ω	Angular velocity
θ	Phase angle

I. INTRODUCTION

Advances in inexpensive control systems and electronic devices have greatly promoted the development of small Unmanned Aerial Vehicles (UAVs) in a wide range of applications [1]. Because of their unique hovering ability (e.g. vertical take-off and landing) and user-friendly flight controllability, the UAVs with rotary-wing system are very attractive to engineers. They offer promising solutions for varieties of civilian applications, such as package delivery, field sites surveillance, disease control, video taking, and personal entertainment. To provide sufficient thrust for small UAVs, multi-rotors are frequently used during various tasks. Example like quadrotor,

¹ Post Doctor, Department of Aerospace Engineering.

² Graduate Student, Department of Aerospace Engineering.

³ Graduate Student, Department of Aerospace Engineering.

⁴ Martin C. Jischke Professor, Dept. of Aerospace Engineering, AIAA Associate Fellow, Email: huhui@iastate.edu

which is one of the most widely-used configurations, can achieve 6 degrees of freedom movement by simply controlling the rotational speeds of multi-rotors [2].

Though UAVs with multi-rotary-wing are promising for the civilian applications, technical improvements are highly needed to extend the operating time and reduce the aeroacoustic noise. To date, the operating time for a small rotary-wing UAV is less than one hour, which is far from enough for complex tasks. One effective method to increase the operation time is to improve the aerodynamic performance of multi-rotary wing in UAVs. Bristeau *et al.* [3], who studied the aerodynamic effects of the propellers and their interactions with the UAV body motion, found that the flexibility of the propellers played an important role in the dynamics of the UAV. To obtain first-hand aerodynamic data of commercial UAVs, Russell *et al.* [4] performed a comprehensive study that quantified the thrusts of five multi-rotor UAVs at various wind speeds, rotor speeds, and vehicle attitudes. Beside aerodynamic performance, the aeroacoustic noise is another issue that needs to be addressed for small UAVs, which not only make people annoying, but also tensed wild animal up. To reduce the broadband noise of a min-UAV propeller, Leslie *et al.* [5] applied a straight transition strip at the leading edge of blade, and found that the leading-edge trip is very effective in reducing the UAV broadband noise. Sinibaldi and Marino [6] experimentally measured the aeroacoustic signatures of two UAV propellers, and found that while the optimized propeller is significantly lower than that of the conventional one at lower value of thrust, the noise of the two propellers would reach a same magnitude when the thrust increased to a higher value.

Multi-rotors UAVs are commonly featured by even number of rotors that are designed into two sets with either clockwise or counter-clockwise rotations. Very few studies can be found in literatures that examined the rotor-to-rotor interactions on the aerodynamic and aeroacoustic performance of UAVs. Except for Yoon *et al.*[7], they computationally analyzed the aerodynamics performance of multi-rotor flows in a quadcopter, and found that the rotor interaction has significant effects on the vertical forces of quadrotor systems in hover motion. And Intaratap *et al.*[8], who experimentally measured the acoustics level of Phantom II at static thrust conditions, found that there is a dramatically increase in acoustic broadband noise if increased the rotors from 2 to 4. Though those previous studies have uncovered the significant impacts of rotor interactions on the aerodynamic and aeroacoustic performance of small UAVs, extensive works are still needed to understand the underlying physics pertinent to multi-rotor interactions, and understand how rotor-to-rotor interactions affect the aerodynamic performance and aeroacoustic noise in small UAVs.

In the present study, in contrast to a single rotor case (i.e., baseline case), a twin-rotor configuration that has two identical rotors (i.e., counter rotating) was used to investigate the effects of rotor-to-rotor interactions on the aerodynamics and aeroacoustic performances of small UAVs. While high-sensitivity force and microphone were utilized to quantify the thrust and noise variations in the twin-rotor case in comparison to that of the baseline, a high-resolution PIV system was used to capture the detailed flow structures and the corresponding vortex evolutions along the induced flow direction. The effects of rotors separation distance (i.e., $L = 0.05D$, $0.1D$, $0.2D$, and $1.0D$, which is $0.04D$ for DJI Phantom 3) on the aerodynamic and aeroacoustic performance of UAVs were examined comprehensively based on the measured forces and noise results. Finally, the detailed flow field measurements were correlated with the thrust and sound results to elucidate the underlying physics in order to explore/optimize design paradigms for better design of next generation multi-rotor drones.

II. TEST MODEL AND EXPERIMENTAL SETUPS

In the present study, the rotor model was made of hard plastic material and manufactured by a rapid prototyping marching (i.e., 3-D printing) that built the UAV model layer-by-layer with a resolution of about 25 microns. Figure 1 shows the schematic of the designed rotor model used in the experiment. The diameter of the rotor is 240 mm ($D = 240$ mm), which can provide a 3.0 Newton thrust at rotation speed of 4860 RPM. It is very similar to the rotor performance of Phantom II. An E63 airfoil shape was selected to generate the rotor blade due to its high lift to drag ratio at low Reynolds number. While the chord length of the rotor blade is set to be 11 mm at the tip, as for the other locations (i.e., from tip to 30% of the blade), they were determined by utilizing the optimal chord length equation $C_r = \frac{C_{tip}}{r}$, where C_{tip} is the chord length at the tip, and r is a non-dimensional radius that is zero at the center and one at the blade tip. Note that, the twist angle of the blade from the tip to 30% of the blade was changing from 10° to 20° . The solidity of the rotor blade is 0.12 in the present study.

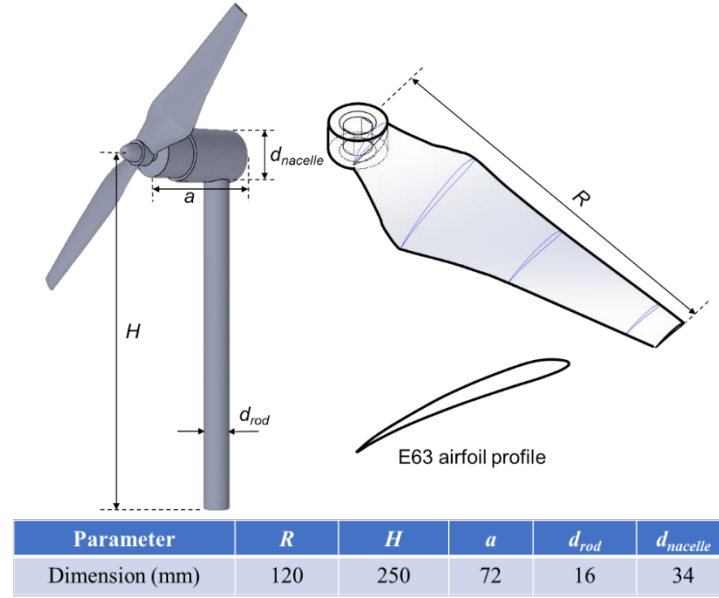


Figure 1. The schematic of the UAV rotor model used in the present study.

The experimental study was performed in the Advanced Flow Diagnostic and Experimental Aerodynamic Laboratory located at the Iowa State University. Figure 2 (a) shows the experimental setup used for the dynamic thrust measurements, where the main test rig is a custom-built 8020 alumina stage. As shown clearly in the figure, an aluminum rod was connected to a high-sensitivity force-moment sensor (JR3 load cell, model 30E12A-I40) to measure the dynamic thrusts of the rotor. The JR3 load cell is composed of foil strain gage bridges, which is capable of measuring the forces and moments on all three orthogonal axes. The precision for force measurements is within $\pm 0.25\%$ for the full range (40 N). While the single rotor case is set to be the baseline, the twin-rotor configuration is achieved by installing another identical rotor nearby. It is important to note that, the twin rotors were mounted on two different stages in order to isolate the aerodynamic interactions effect on the thrust measurements from the mechanical vibration caused by the second rotor. During the experiment, the separation distance (L) within rotor tips was varying from $0.05D$ to $1.0D$ to study the multi-rotor interactions on the aerodynamic and aeroacoustic performance of UAV rotor. The JR3 was used to measure the dynamic load acting on the rotor, meanwhile a Monarch Instrument Tachometer was used to monitor the rotor rotating speed. The dynamic thrust for each case was acquired at a sampling rate of 3000 Hz for 120s.

In addition to the dynamic load measurement, an aeroacoustic sound measurement was conducted in an anechoic chamber located at Iowa State University. The chamber has physical dimensions of $12 \times 12 \times 9$ feet with a background noise level lower than 20dB, where the reference sound pressure is $20 \mu\text{Pa}$. Figure 2 (b) shows the experimental setup for the aeroacoustic noise measurement in the present study. In order to measure the aeroacoustic sound of twin-rotors, a high-accuracy microphone was placed $6D$ away from the center point of the twin-rotor system. The measurement was performed at 5 different angular positions with every 30° interval, starting from the front position of twin-rotor to 30° behind the rotors. Each sound measurement was recorded for 120s.

Finally, a high-resolution PIV system was used to conduct detailed flow field measurements to quantify the dynamic interactions between the rotor and induced flow, shown in Fig. 2 (a). During the experiment, the air flow was seeded with $\sim 1 \mu\text{m}$ oil droplets generated by droplet generator. Illumination was provided by a double-pulsed Nd:YAG laser (NewWave Gemini 200), adjusted on the second harmonic and emitting two pulses of 200 mJ with the wavelength of 532 nm at a repetition rate of 2 Hz. Using a set of high-energy mirrors and optical lenses, the laser beam was shaped into a thin light sheet with thickness of about 1.0 mm in the measurement interest. The illuminating laser sheet was firstly aligned horizontally along the induced flow direction, bisecting the hub in the middle of the rotor, to perform 2D PIV measurements in the X-Z plane. Then, the laser sheet was rotated 90° to perform stereoscopic PIV (SPIV) measurements at different downstream locations behind rotors to reveal the vortex structures in the X-Y planes.

As for the SPIV experiment, two high-resolution 14-bit high-resolution CCD cameras (PCO2000, Cooke Corp.) were used for the image acquisitions. The two cameras were arranged with an angular displacement configuration of about 45 degrees to get a largely overlapped view. With the installation of tilt-axis mounts, laser illumination plane, the lenses and camera bodies were adjusted to satisfy the Scheimpflug condition. The CCD cameras and double-pulsed Nd:YAG laser were both connected to a Digital Delay Generator (Berkeley Nucleonics, Model 565) to control the timing of the lasers and image acquisitions. A general in-situ calibration procedure was conducted to obtain the mapping functions between the image planes and object planes for the SPIV measurements. A target plate ($\sim 350 \times 350 \text{ mm}^2$) with 2 mm diameter dots spaced at intervals of 8 mm was used for the in-situ calibration. The mapping function used in the present study was a multi-dimensional polynomial function, which is third order for the directions parallel to the laser illumination plane (i.e., X and Y directions), and second order for the direction normal to the laser sheet plane (i.e., Z direction). For the 2D PIV measurements, the instantaneous flow velocity vectors were obtained by using a frame-to-frame cross-correlation technique to process the acquired PIV images with an interrogation window size of 32 pixels \times 32 pixels. An effective overlap of 50% of the interrogation windows was employed in PIV image processing, which resulted in a spatial resolution of 2.3 mm (i.e., $0.01D$) for the PIV measurement results. Similar process methodology was also used for the SPIV image processing. The instantaneous 2D velocity vectors were then used to reconstruct all three components of the flow velocity vectors in the laser illuminating plane by using the mapping functions obtained through the calibration procedure. After the instantaneous flow velocity vectors (u_i, v_i, w_i) were determined, the distributions of the ensemble-averaged flow quantities such as mean velocity (U, V, W), normalized turbulence kinetic energy ($0.5(\overline{u^2} + \overline{v^2} + \overline{w^2})/U_\infty^2$), spanwise vorticity ($\omega_y = \frac{\partial u_i}{\partial z} - \frac{\partial w_i}{\partial x}$) for the 2D PIV measurements, and streamwise vorticity ($\omega_z = \frac{\partial v_i}{\partial x} - \frac{\partial u_i}{\partial y}$) for the SPIV measurements were obtained from a sequence of 1,000 frames of instantaneous PIV measurement results. The uncertainty level for the PIV measurements is estimated to be within 3% for the instantaneous velocity vectors, while the uncertainties for the measured ensemble-averaged flow quantities such as vorticity distributions are about 10%.

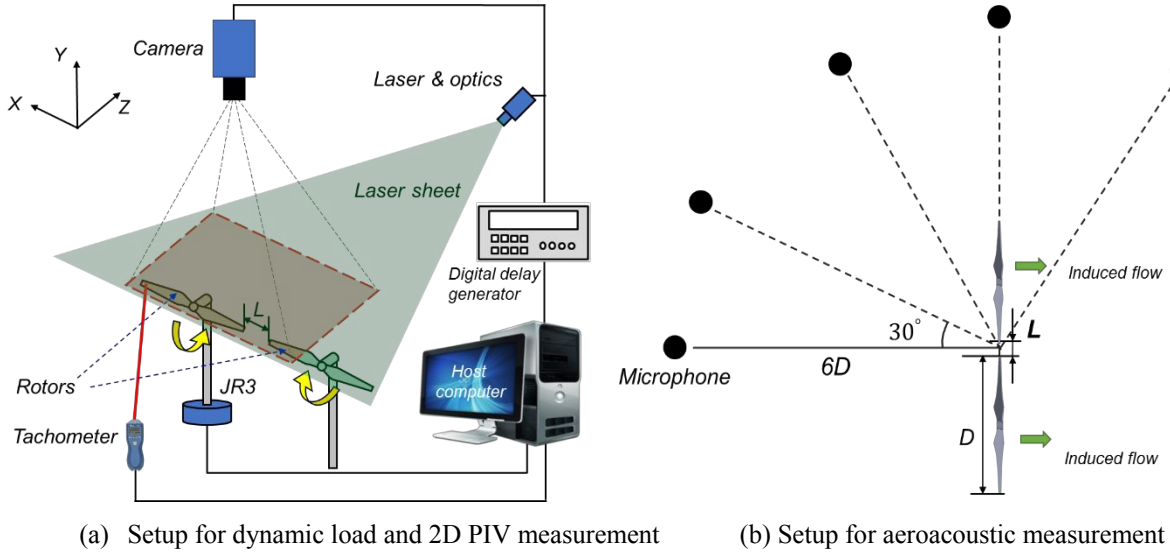


Figure 2. Experimental setups for rotor-to-rotor interactions study.

III. Measurement Results and Discussions

A. Dynamic load measurement results

Figure 3 shows the measured normalized thrust coefficient and standard deviation of designed rotor as a function of separation distance, where the thrust coefficient (i.e., $C_T = \frac{4T}{\rho n^2 D^4 \pi^3}$) and standard deviation were normalized by the corresponding quantities of the single rotor case, which are 0.013 and 0.21 Newton respectively. During the experiment, while the rotation speed (n) of individual rotor was maintained at 81Hz, the separation distance between rotor tips was adjusting from $L/D = 0.05$ to 1.0. As shown clearly in Fig. 3, though the separation distance was shortened by a factor of 10, the measured thrust coefficient for the twin-rotor cases was found to drop by less than 2%, which suggests that the generated mean thrust is independent of the separation distance. Similar results were also reported by Yoon *et al.*[7], who performed a computational study on the aerodynamic interactions of multi-rotor flows. While the separation distance had limit effect on the thrust coefficient of rotor, the force fluctuations (i.e., thrust standard deviation) were found to increase dramatically as the separation distance becomes smaller. More specifically, the measured thrust fluctuations for the $L = 0.05D$ case was found to be ~ 2.5 times larger than that of the $L = 1.0D$ case. Since these rotors were mounted on two separated stages, the significant augmentation in force fluctuation for the $L = 0.05D$ case was believed to be only caused by the intensified rotor-to-rotor interactions rather than mechanical vibrations induced by the second rotor. It should also be noted that, as the separation distance became larger than $0.5D$, the measured thrust fluctuation for twin-rotor case would mitigate greatly and eventually reach a similar level with that of the single rotor case. In general, the effect of rotor interactions on the aerodynamic performance of small UAV becomes negligible if the separation distance is larger than one diameter of the rotor blade.

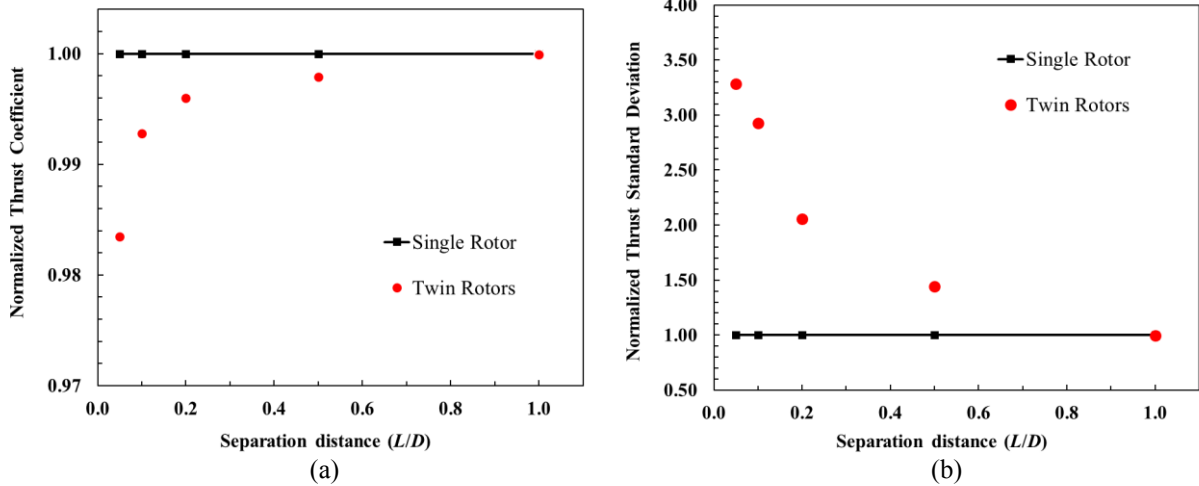


Figure 3. Effects of separation distance on the thrust coefficient (a) and standard deviation (b) of UAV rotor, where the thrust coefficient and standard deviation of the single rotor case are 0.013 and 0.21 N, respectively.

B. Sound measurement results

Besides the dynamic load measurement, an aeroacoustic noise measurement was conducted in an anechoic chamber located at Iowa State University. Figure 4 depicts the sound pressure level (i.e., SPL) distribution at $6D$ away from the center of the twin-rotor system, which can be approximately treated as far-field location, where the microphone was oriented at five different azimuthal angles (i.e., $\beta = 60^\circ, 90^\circ, 120^\circ, 150^\circ, 180^\circ$). Note that, the sound pressure levels plotted in Fig. 4 were the integration of frequency energy starting from 20 Hz to 20,000 Hz. It is well-known that, the noise distribution around single rotor is symmetric along the rotor plane (i.e., dipole distribution), which would reach a maximum noise level at positions right ahead or behind the rotor (i.e., $\beta = 0^\circ, 180^\circ$) but minimum noise at the side locations (i.e., $\beta = 90^\circ, 270^\circ$). This agrees with the measured results shown in Fig. 4, that the measured SPLs for the twin-rotor configuration were found to increase monotonously as the azimuthal angles increase from 90° to 180° . Not only that, but also the noise level at $\beta = 60^\circ$ was found to be

approximately same with that of $\beta = 120^\circ$, which confirmed that the SPL is symmetric along the rotor plane. It should also be noted that, as the separation distance decrease, the measured SPLs were found to increase gradually behind the rotors. A maximum enhancement of about 3 dB can be observed for the $L = 0.05D$ case in comparison to the $L = 1.0D$ case at the azimuthal angle of $\beta = 180^\circ$, which is believed to be caused by the enhanced rotor-to-rotor interactions. Therefore, the measured sound is a function of both azimuthal angle and separation distance that the SPL increases as the separation distance decreases.

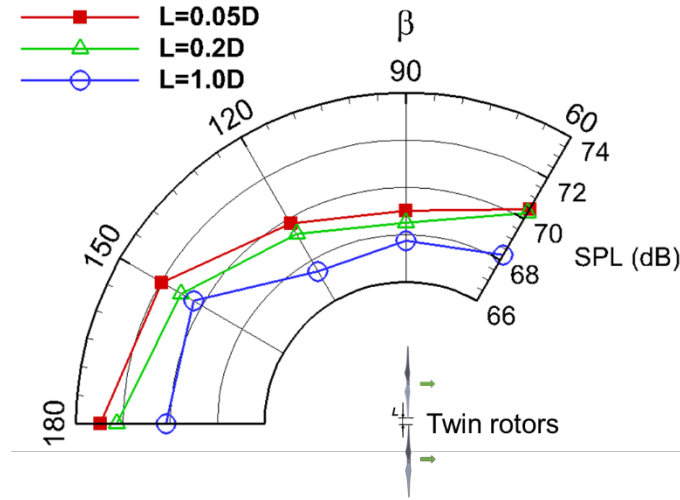


Figure 4. Sound pressure level distributions at $6D$ away from the center of the twin-rotor configuration.

Though results from Fig. 4 indicated that the measured SPL increased as the separation distance decreased, it is still unclear whether the noise increase is due to the enhancement in tonal noise, broadband noise, or both. Therefore, it is necessary to perform a sound spectrum analysis at various locations. Figure 5 shows the measured sound spectrums as a function of blade passing frequency harmonics at azimuthal angles of $\beta = 120^\circ, 180^\circ$. As shown clearly in Fig. 5, the SPLs for the $L = 0.05D$ case were found to be much higher than that of the $L = 1.0D$ case at the integral multiple of BPF (i.e., BPF, BPF2...), indicating an enhanced tonal noise component behind the UAV rotors. Note that, the high sparks at BPF ≈ 20 were confirmed to be the signal from the electronic motors, which were used to drive the rotors during the experiment. For incompressible flow condition, the tonal noise is dominated by the loading noise [9], which is directly associated with the dynamic loading of the rotor blade. Therefore, the augmentation of tonal noise for the $L = 0.05D$ case is believed to be caused by the intensified thrust fluctuations as mentioned in Fig. 3 in comparison with that of the $L = 1.0D$ case.

In addition, comparing to the $L = 1.0D$ case, the broadband noises for the $L = 0.05D$ were found to increase mildly at the azimuthal angles of $\beta = 120^\circ, 180^\circ$. Recalling the Lighthill's stress tensor [9], the broadband noise level is largely determined by the complex turbulent flow structures and shear layers, such as secondary flow distortions, blade trailing edge vortices, and tip vortices. As suggested by Carolus et al. [10], the turbulent kinetic energy (TKE) and force fluctuations are important parameters that can be used to evaluate the level of broadband noise. Thus, the measured noises in Fig. 5 indicates that the flow behind the UAV rotors could probably features with increased TKE level and force fluctuations as the separation distance decreased, while the augmentation of force fluctuation has already been confirmed by the results shown in Fig. 3.

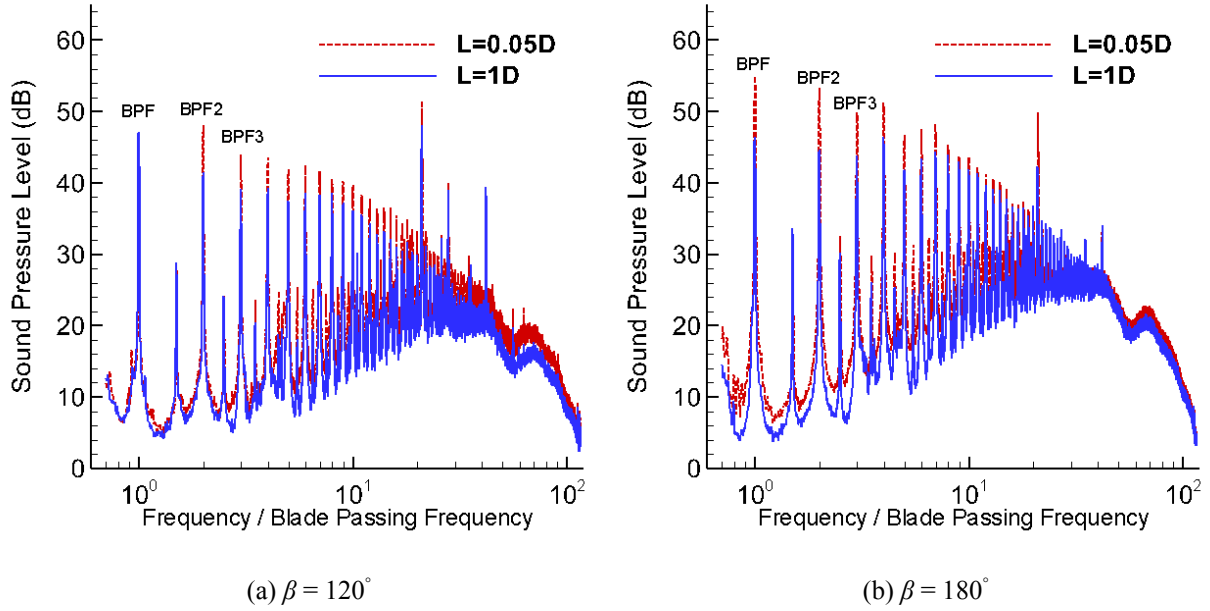


Figure 5. Comparison of the measured sound spectrum between the $L = 0.05D$ case and the $L = 1.0D$ case at azimuthal angles of 120° and 180° .

C. Free-run PIV measurement results

As mentioned above, a free-run PIV measurements were conducted in the present study to understand how the rotor-to-rotor interactions affect the aerodynamic and aeroacoustic performance of small UAV. Figure 6 shows the measured free-run PIV results in term of ensemble-averaged flow velocity and normalized in-plane turbulence kinetic energy ($0.5(\overline{u'^2} + \overline{w'^2})/U_{tip}^2$) for the single and twin-rotor cases, where the rotor tip speed (i.e., $U_{tip} = \omega D/2$) is 61 m/s. As shown quantitatively in Fig. 6 (a), the ensemble-averaged velocity distribution behind the twin-rotor case was found to be similar with that of the single rotor case, which agrees with the measured mean thrust results as shown in Fig. 3(a). During this process, the high-velocity region was found to converge from around the blade tip location (i.e., $0.4D$) to near the root position (i.e., $0.3D$) as the main flow convected downstream. The significant radial contraction of the induced flow (i.e., W component) behind the rotors was clearly evident in both cases. While the global features of the velocity distribution behind the rotors were found to be similar for both cases, some differences can be identified from the comparison of the velocity distribution fields. Comparing to the single rotor case, the measured velocity field in the twin-rotor case was found to be slightly ‘dragged’ down toward the adjacent rotor, which is believed to be caused by the Coanda effect (i.e., a phenomenon in which a flow tends to attract to a nearby object). As a result, the W velocity component behind the twin-rotor was found to be slightly lower than that of the corresponding single rotor case in the down-part region ($-0.5 < X/D < -0.2$).

Fig. 6 (b) shows the normalized in-plane TKE distribution for the single and twin-rotor cases. Clearly, for the single rotor case, regions near the rotor tips were characterized with elevated in-plane TKE, which is caused by the periodic vortex shedding from the blade tip. Similar phenomenon can be observed for the twin-rotor case, except the in-plane TKE level within the rotor interaction region was found to be higher than that of the single rotor case at the corresponding region. Since the two rotors were only $0.05D$ apart, the tip vortexes from rotors would interact severely with the nearby vortex structures, rendering enhanced in-plane TKE distribution in contrast to the single rotor case. This phenomenon is believed to be not only related to the significant enhancement of thrust fluctuations in the twin-rotor case (i.e., shown in Fig. 3), but also tie to the augmentation of broadband noise (i.e., shown in Fig. 5), which will discuss further in the following Stereoscopic PIV results.

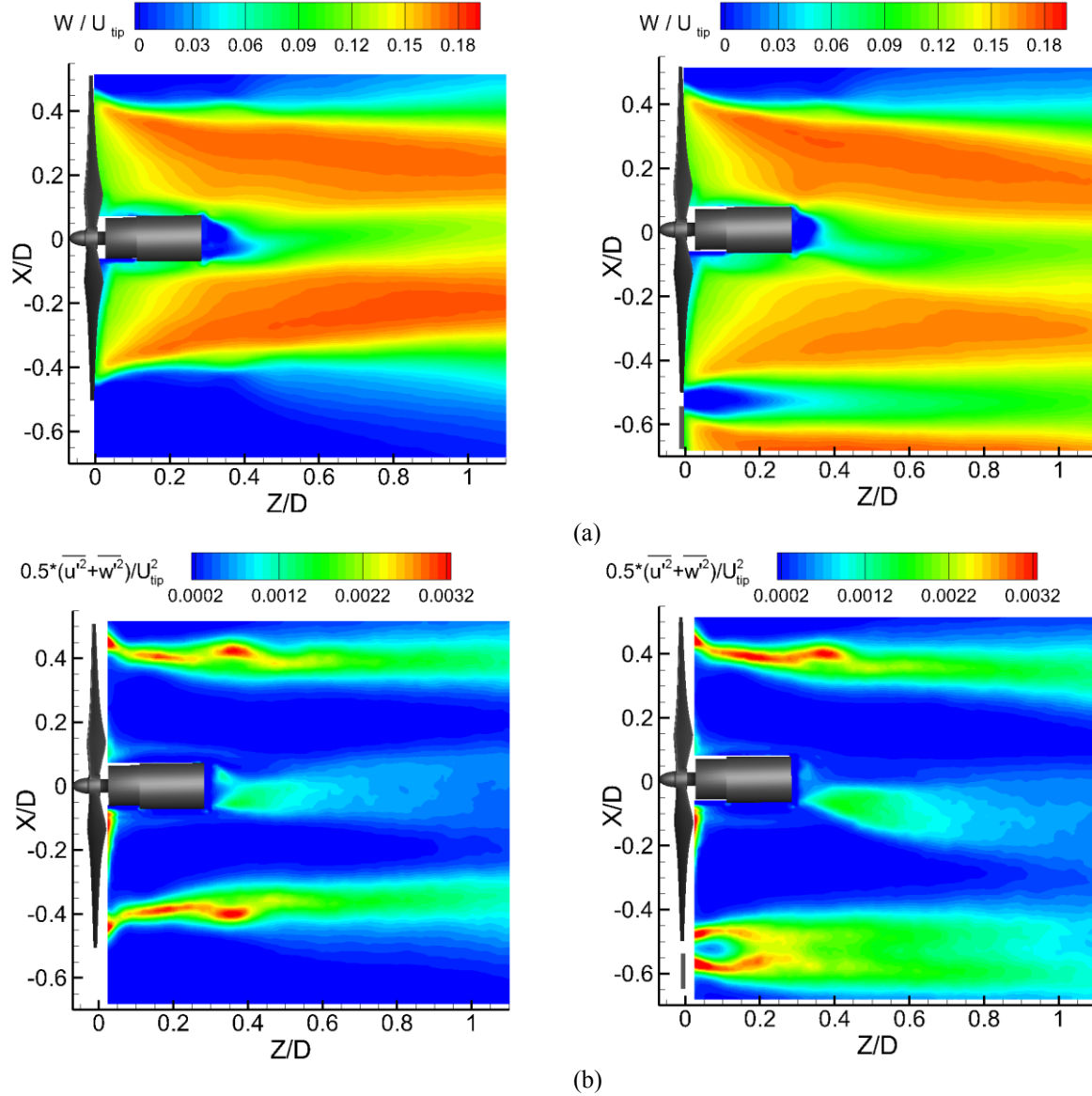


Figure 6. Measured PIV results for the single rotor (left) and twin-rotor (right, $L=0.05D$) cases: (a) Ensemble-averaged velocity field, (b) Normalized in-plane TKE distribution.

D. Phase-locked PIV measurement results

In the present study, phase-locked PIV measurements were also employed to produce “frozen” images of the unsteady vortex structures in the rotor wake at different phase angles. Note that, only the phase of the main rotor in the twin-rotor configuration was monitored during the phase-locked PIV test, whereas the other rotor can be treated as free-run condition. Figure 7 shows the comparison of phase-averaged velocity distributions between the single and twin-rotor case at two different phase angles (i.e., $\theta = 0^\circ, 120^\circ$). During the experiment, the phase angle is defined as the angle between the vertical Y - Z plane and the position of a pre-marked rotor blade. The pre-marked blade was in the most upward position (i.e., within the vertical Y - Z plane) for the phase angle of $\theta = 0^\circ$. As shown in Figure 7, the existence of wave-shaped flow structures can be observed clearly at the tip-top height for the single rotor case, which is closely related to the periodical shedding of tip vortices behind the rotor. These wave-shaped flow structures would propagate downstream as the phase angle increases. However, due to the rotor interactions within the twin-rotor case, the wave-shaped structures were found to dissipate much faster and become less

pronounced within the gap region in comparison with that of the single rotor case. In addition, these flow structures behind rotors were found to shift radially downward to the adjacent rotor, which is consisted with the measured results as shown in Fig. 6.

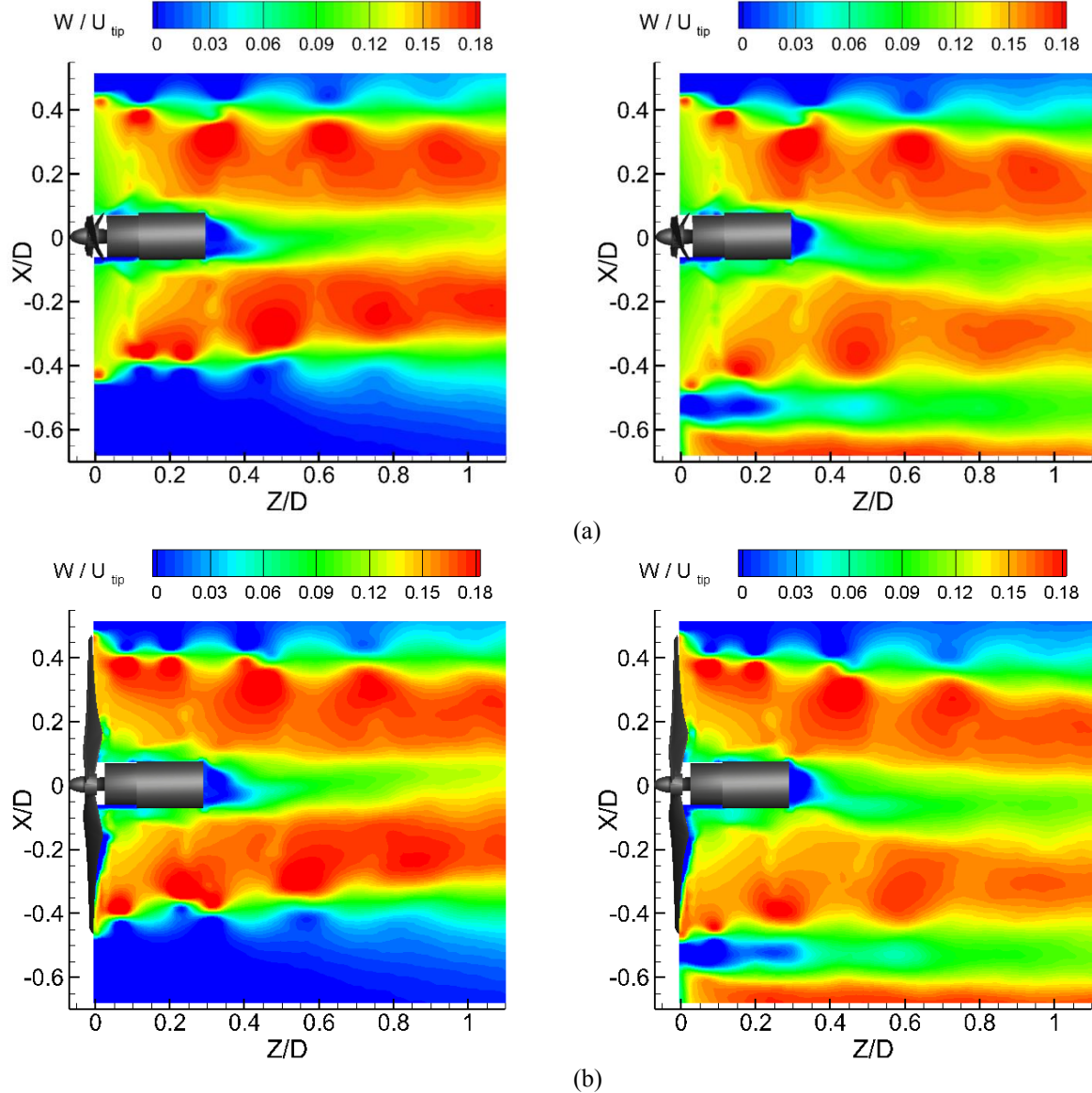


Figure 7. Phase-locked flow velocity distributions for the single rotor (left) and twin rotors (right, $L=0.05D$) configuration: (a) Phase angle $\theta = 0^\circ$, (b) Phase angle $\theta = 120^\circ$.

Figure 8 shows the comparison of phase-locked vorticity distributions between the single rotor and twin-rotor cases, which can be used to reveal the effect of rotor interactions on the unsteady vortices more clearly, where the separation distance is $0.05D$. It is as expected, the general features of the vorticity distributions were found to be quite similar for both cases, especially for the upper-part region (i.e., as indicated using red dash line). Flows behind the rotors were featured by pairs of tip vortices (i.e., **1 - 5**) and shear layers (i.e., **a - d**) that trailed after the blades. Note that, the tip vortices were formed because of the pressure difference within the blade, while the shear layers were generated due to the merging of boundary layers from the upper and lower surfaces of the blade.

For the single rotor case, when the pre-marked blade rotated over the PIV measurement plane, a tip vortex was found to be shed from the tip and then propagate axially downstream, shown in Fig. 8 (a). During this process, pairs

of vortex structures (i.e., such as vortex **4** with vortex **3**, vortex **2** with vortex **1**) would slowly merge into an integral one at $\sim 0.7D$ as the flow convected downstream, then completely vanish beyond $1.0D$ due to the aperiodic and highly turbulent in the wake further downstream. As for the twin-rotor case (i.e., $L = 0.05D$), though similar distributions can be observed for the shear layer (i.e., **a** – **d**), the tip vortices were found to merge and dissipate much faster in comparison with that of the single rotor case. Representative examples are the isolated vortices (i.e., **1**, **2**, **3**, **4**), shown in the case of twin-rotor, that become much harder to discern as $Z/D > 0.2$.

As the phase angle increased to $\theta = 120^\circ$, the associated turbulent structures, such as the shear layers and tip vortices, were found to propagate downstream in comparison with that of Fig. 8 (a). Focusing on the evolution of vortex sheet **d** (i.e., shear layer **d**) behind both cases, it was initially adjacent to the tip vortex **4**. As both tip vortex and sheet convect axially downstream, however the outboard edge of the shear layer **d** in Fig. 8 (b) was found to interact with the tip vortex **3** rather than vortex **4**. This is because the convecting speed (i.e., W velocity shown in Fig. 7) of shear layer was significantly higher than that of the tip vortex, therefore the outboard edge of shear layer surpassed the corresponding vortex, leading to a complex interaction between vortex structures. Very similar phenomenon was also reported by Leishman [11], who described the wake characteristics behind a helicopter rotor.

E. Stereoscopic PIV measurement results

To further explore the underlying physics pertinent to rotor-to-rotor interactions of small UAV, a stereoscopic PIV (SPIV) system was also utilized to quantify the complex flow field behind the rotors at multiple locations along the induced flow direction. Note that, the vectors shown in Figure 7 and 8 are the resultant vectors of in-plane radial and tangential velocities behind the rotor.

Fig. 9 and Fig. 10 shows the comparisons of ensemble-averaged turbulent quantities between the single rotor and twin-rotor cases by employing SPIV technique at the downstream location of $X/D = 0.1$ and 1.0 , respectively. As revealed clearly in Fig. 9 (a), the mean velocity contour (i.e., W component) behind the single rotor was found to be circular and symmetric as expected. Due to the continuous driving of rotor, the wake flow would rotate in the same direction with that of the rotor blade (i.e., both in counter-clockwise), which is contrary to the wind turbine scenario [12] that the swirling wake is opposite to the turbine rotating direction. This is caused by the inherent working mechanism difference that, the rotor drives the flow in the UAV case, however, as for the wind turbine, it is the flow that drives the rotor. It should also be noted that, while the velocity distribution behind the single rotor was in circular shape, a droplet-shaped velocity field was observed for the twin-rotor case due to the flow disturbance from the nearby rotor. Carefully inspecting the flow features behind the twin-rotor case, a region with flow separation was identified at the top-right corner, which is believed to be the resultant effect of upwash flow and radial flow. Within the interaction region, the two rotors would generate a steady upwash flow that interacts severely with the radial flow of rotor, resulting in flow separation as shown in Fig. 9 (a).

As the airflow moved further downstream to the $X/D = 1.0$ plane, shown in Figure 10, the previous circular-shaped velocity field behind the single rotor was found to transform into a ‘horseshoe’ shape. Not only that but also the orientation of the velocity contour was found to rotate $\sim 35^\circ$ from its original vertical position (i.e., $X/D = 0.1$ plane). Due to the flow inertial, the air stream after speeding up by the rotating blade would continue to rotate as it travels further downstream. While a similar swirling angle was observed for the twin-rotor case, the velocity contour was found to bend slightly toward the adjacent rotor in comparison with the baseline, especially for the region close to the flow separation region (i.e., region in black dash line). It should also be noted that, comparing to the single rotor case, the vortex core was also found to be attracted to the nearby rotor. These phenomena are believed to be closely related to the afore mentioned Coanda effect (i.e., Fig. 6) that the induced airflow behind the twin rotors would be attracted and bent toward the nearby rotor.

Fig. 9 (b) shows the measured normalized TKE distributions ($0.5(\overline{u^2} + \overline{v^2} + \overline{w^2})/U_{tip}^2$) for the single rotor case in comparison with that of the twin-rotor case in the $X/D = 0.1$ plane. Clearly, an O-ring shaped TKE distribution was found to be the dominant feature for the single rotor case, which is caused by the periodic vortex shedding from

the rotor tip. The measured results are in accordance with the measured 2D PIV results shown in Fig. 6. With the existence of the second rotor, while the general TKE distribution for the two cases was found to be similar, a region with significant higher TKE level was identified at the up-right location for the twin-rotor case. As expected, the region with separated flow would lead to greatly enhanced turbulence fluctuations (i.e., TKE), which consequently results in dramatically intensified force fluctuations for the twin-rotor case as mentioned in Fig. 3 (b). This also verified the conjecture that the enhanced broadband noise shown in Fig. 5 was caused by the augmented TKE level. Imagine that, as the blade struck through the separation region, it would certainly suffer strong fluctuations, leading to augmented TKE and broadband noise distribution in comparison with that of the baseline case. As for the normalized TKE distributions shown in Fig. 10 (b), the measured TKE levels for both cases were found to decrease gradually due to the viscous effect within shear layer.

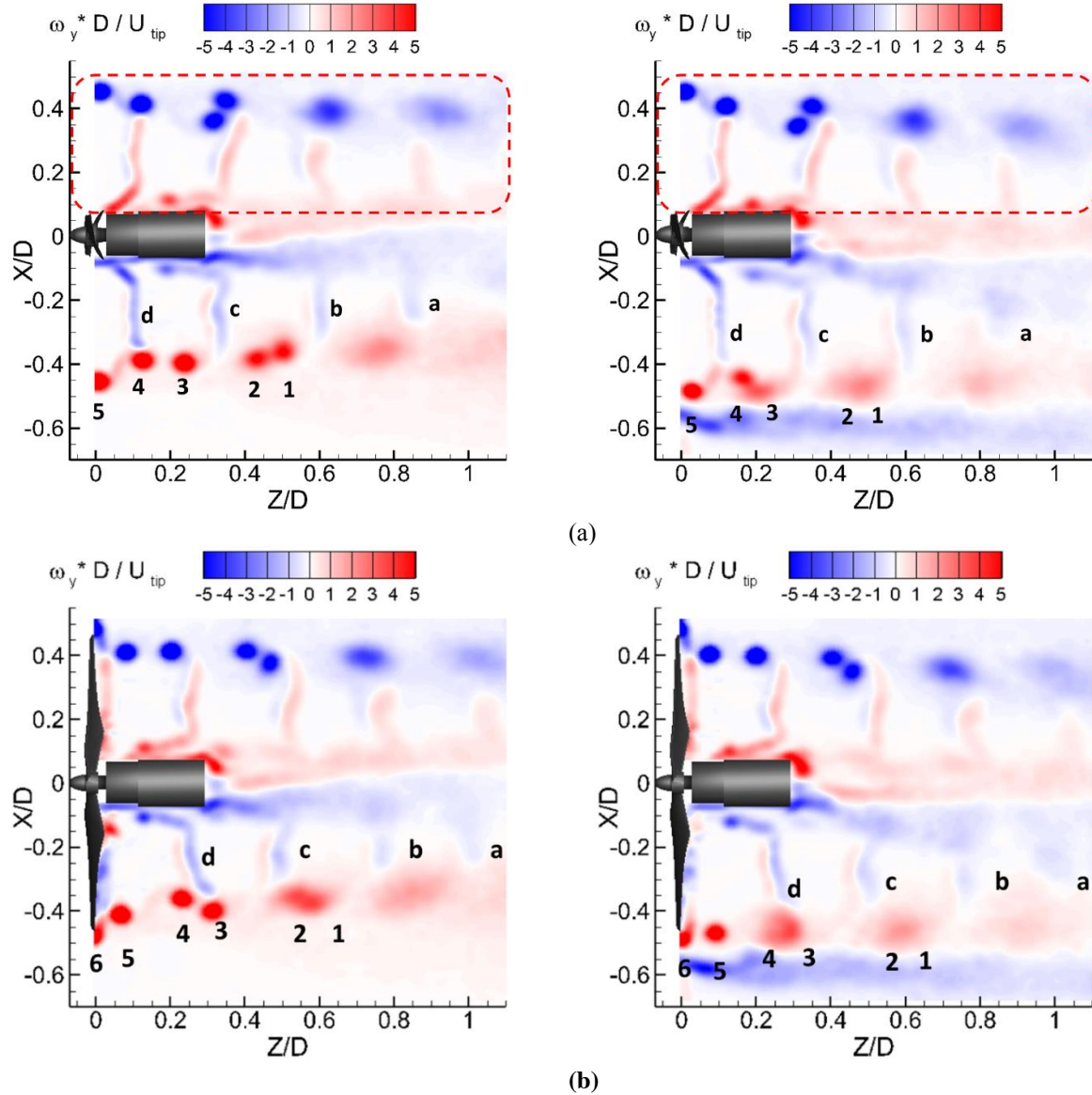


Figure 8. Phase-locked vorticity distributions for the single rotor (left) and twin rotors (right, $L=0.05D$) configurations: (a) Phase angle $\theta = 0^\circ$, (b) Phase angle $\theta = 120^\circ$.

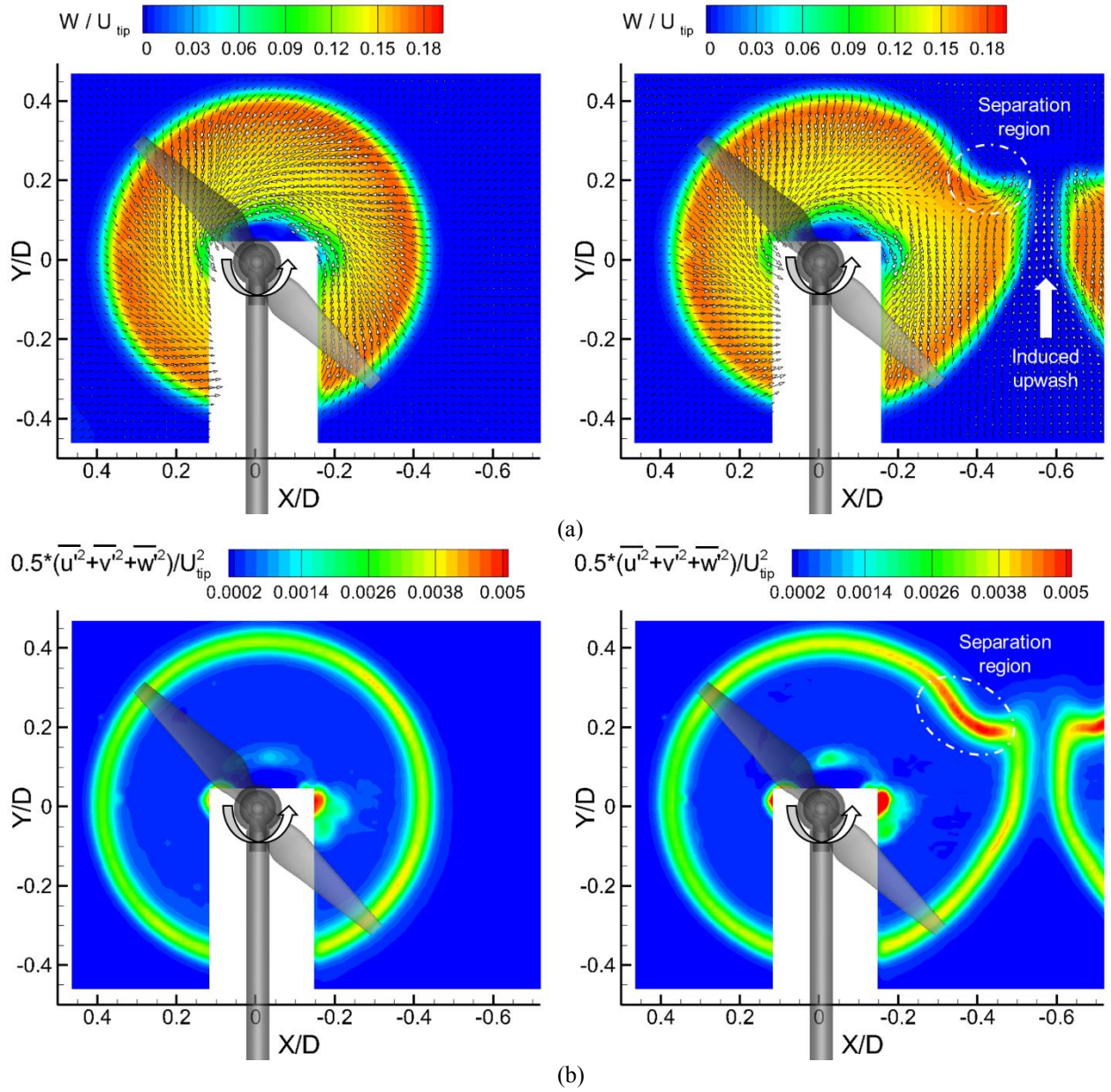


Figure 9. Measured SPIV results for the single rotor (left) and twin-rotor (right, $L=0.05D$) configurations in the $X/D = 0.1$ cross plane: (a) Ensemble-averaged velocity field, (b) Normalized TKE distribution.

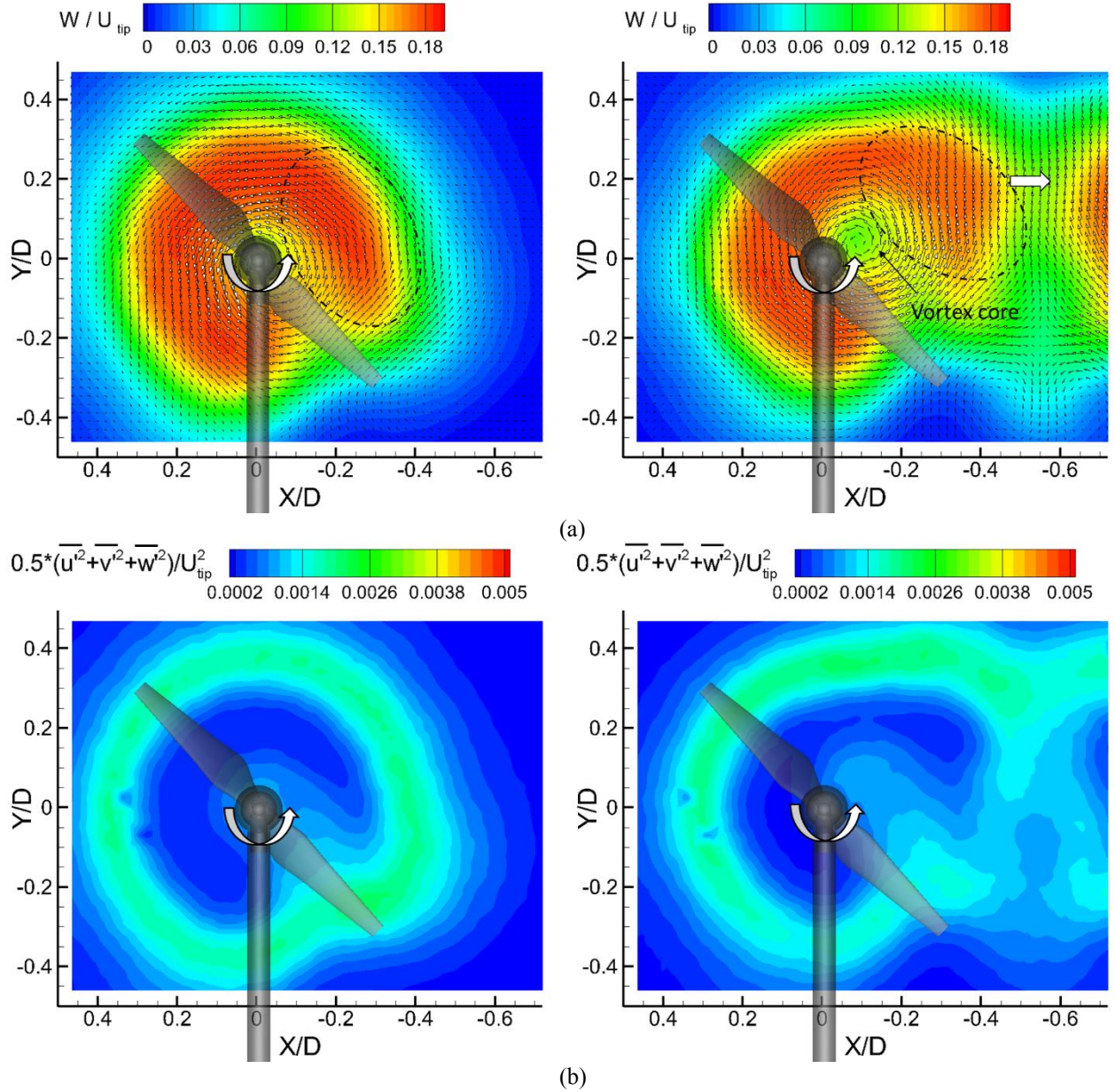


Figure 10. Stereoscopic PIV results for the single rotor (left) and twin-rotor (right, $L=0.05D$) configurations in the $X/D = 1.0$ cross plane: (a) Ensemble-averaged velocity field, (b) Normalized TKE distribution.

Figure 11 shows the evolution of ensemble-averaged streamwise velocity and normalized TKE distributions for the single and twin-rotor cases at three typical streamwise locations (i.e., $X/D = 0.1, 0.5$, and 1.0). As shown clearly in the figure, as induced flow convected downstream, the ensemble-averaged velocity fields for both cases were found to become more uniform due to the shrinking of flow area. In addition, the orientation of the induced flows was found to rotate approximately 35° (i.e., in the plane of $X/D = 0.1$) in comparison with its original vertical position (i.e., in the plane of $X/D = 1.0$). The normalized TKE distributions given in Fig. 11 (b) reveal clearly that, the magnitude of N.TKE for both single and twin-rotor cases were found to gradually decrease due to the viscous dissipation within the shear layer.

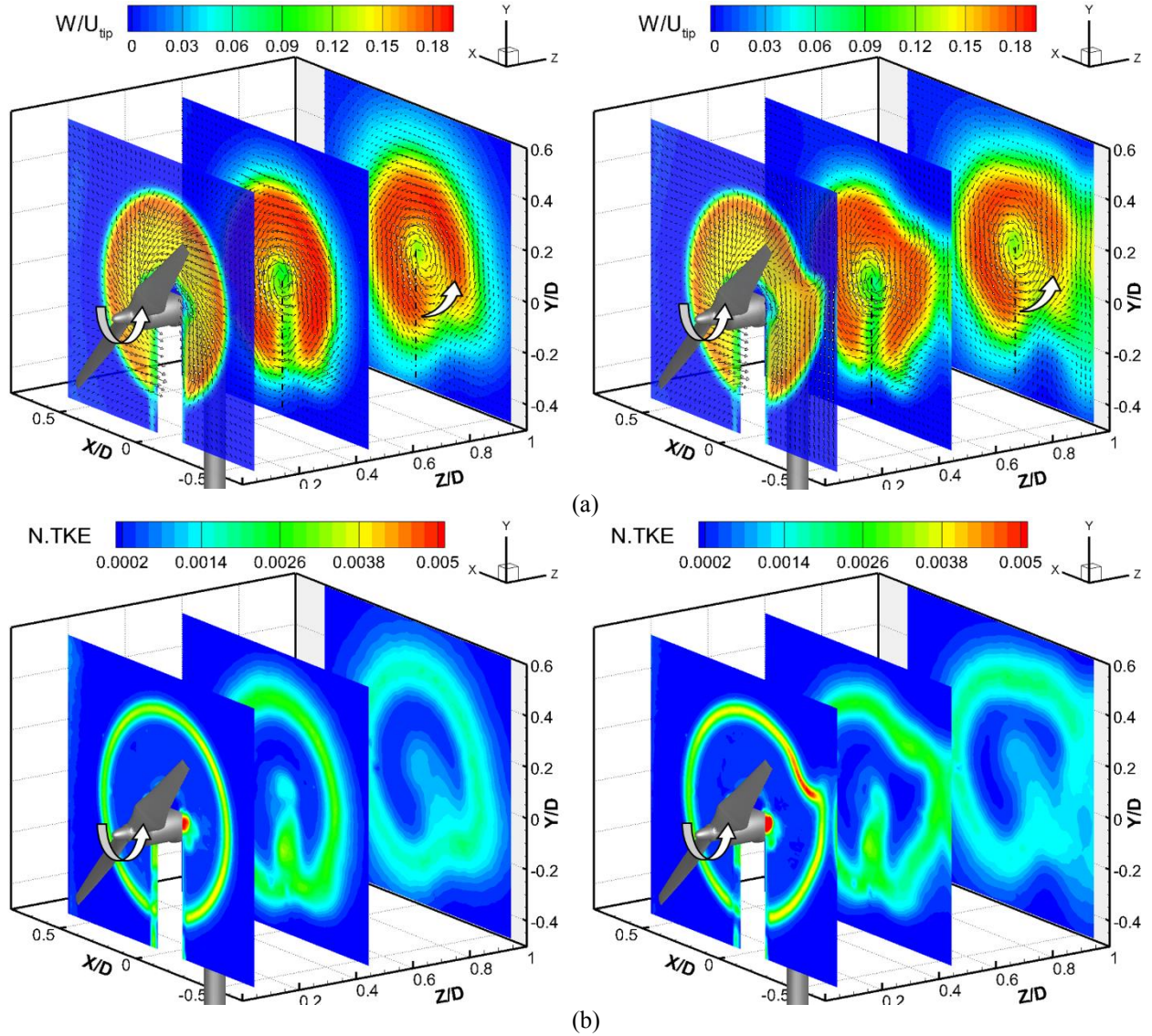


Figure 11. Stereoscopic PIV results for the single rotor (left) and twin rotors (right, $L=0.05D$) configurations at $X/D = 0.1, 0.5$, and 1.0 locations: (a) Ensemble-averaged velocity field, (b) Normalized TKE distribution.

IV. Conclusions

An experimental investigation was performed to study the effects of rotor-to-rotor interactions on the aerodynamic and aeroacoustic performances of small UAVs. While JR3 force transducer and microphone were used to quantify the thrust and noise of the single and twin-rotor cases, a high-resolution Particle Image Velocimetry (PIV) system was used to conduct detailed flow field measurements to reveal the dynamic interactions between the rotors. The effects of separation distance ($L = 0.05D, 0.1D, 0.2D$, and $1.0D$) on the aerodynamic and aeroacoustic performance of UAVs were evaluated in great detail based on the quantitative force, noise, and PIV measurements.

It was found that, while the separation distance had very little effect on the thrust coefficient of the rotor (i.e., variation within 2% for all test cases), the thrust fluctuations (i.e., thrust standard deviation) were found to increase dramatically as the separation distance becomes smaller. More specifically, the measured thrust fluctuations for the twin-rotor case (i.e., $L = 0.05D$) case was found to be ~ 2.5 times larger than that of the baseline case. This is believed to be caused by the complex flow interactions within rotors as revealed by the detailed PIV measurements.

It was also found that, the noise distribution for the twin-rotor case is a function of both azimuthal angle and separation distance, where the measured noise was found to increase as the azimuthal angle increased from 90° (i.e., side position) to 180° (i.e., right behind rotors), and to increase as the separation distance reduced from $L = 1.0D$ to $L = 0.05D$. A maximum noise enhancement of ~ 3 dB can be observed for the $L = 0.05D$ case in comparison to that of the $L = 1.0D$ case, which is the results of both tonal and broadband noise augmentations as indicated in the sound spectrum analysis.

As shown quantitatively from the 2D PIV and Stereoscopic PIV measurement results, the induced flow behind the rotors was found to contract radially toward the axis of rotor as flow convected downstream. For the single rotor case, while most of the regions in the wake were devoid of flow structures, only the region near the blade tips was characterized by elevated level of in-plane TKE (i.e., in X - Z plane) due to the periodic tip vortex shedding. Similar phenomenon was observed for the twin-rotor case, except a significant higher TKE region was found at the top-right area in comparison with that of single rotor case. Due to the resultant effect of upwash and radial flows in the near wake of the twin-rotor case, a region with flow separation was identified in the X - Y cross plane, which led to significantly higher TKE distributions and thrust fluctuations behind the twin rotors. It should also be noted that, comparing to the single rotor case, the velocity field for the twin-rotor case was found to be attracted and bent toward the nearby rotor, which is because of the Coanda effect that the induced airflow was dragged toward the nearby rotor.

In general, the measured quantitative results given in the present study are believed to be very beneficial in understanding how the rotor-to-rotor interactions affect the aerodynamic and aeroacoustic performance of small UAV, which depicted a vivid picture about the complex flow features behind the rotors and their correlations with the enhanced force fluctuations and noise level. Such quantitative information is highly desirable to elucidate the underlying physics to gain further insight into the rotor interactions of small UAV and to explore/optimize design paradigms for better UAV designs to extend the operation time and decrease the aeroacoustic noise of commercial UAV.

Acknowledgments

The research work was supported by National Science Foundation (NSF) under award number of IRES-1064235. The authors also want to thank Mr. Linkai Li and Mr. Brandon Weigel of Iowa State University for their help in conducting the experiments.

References

- [1] S. Bouabdallah, M. Becker, R. Siegwart, Autonomous miniature flying robots: coming soon! - Research, Development, and Results, *IEEE Robot. Autom. Mag.* 14 (2007) 88–98. doi:10.1109/MRA.2007.901323.
- [2] H. Otsuka, K. Nagatani, Thrust loss saving design of overlapping rotor arrangement on small multirotor unmanned aerial vehicles, in: 2016 IEEE Int. Conf. Robot. Autom., IEEE, 2016: pp. 3242–3248. doi:10.1109/ICRA.2016.7487494.
- [3] P. Bristeau, P. Martin, E. Salaün, The role of propeller aerodynamics in the model of a quadrotor UAV, in: Control Conf. (ECC, 2009. <http://ieeexplore.ieee.org/abstract/document/7074482/> (accessed April 16, 2017).
- [4] C. Russell, J. Jung, G. Willink, B. Glasner, Wind Tunnel and Hover Performance Test Results for Multicopter UAS Vehicles, in: AHS 72nd Annu. Forum, FL, 2016.
- [5] A. Leslie, K.C. Wong, D. Auld, Broadband Noise Reduction on a mini-UAV Propeller, in: 14th AIAA/CEAS Aeroacoustics Conf. (29th AIAA Aeroacoustics Conf., American Institute of Aeronautics and Astronautics, Reston, Virginia, 2008. doi:10.2514/6.2008-3069.

- [6] G. Sinibaldi, L. Marino, Experimental analysis on the noise of propellers for small UAV, *Appl. Acoust.* 74 (2013) 79–88. doi:10.1016/j.apacoust.2012.06.011.
- [7] S. Yoon, H.C. Lee, T.H. Pulliam, Computational Analysis of Multi-Rotor Flows, in: 54th AIAA Aerosp. Sci. Meet., American Institute of Aeronautics and Astronautics, Reston, Virginia, 2016. doi:10.2514/6.2016-0812.
- [8] N. Intaratep, W.N. Alexander, W.J. Devenport, S.M. Grace, A. Dropkin, Experimental Study of Quadcopter Acoustics and Performance at Static Thrust Conditions, in: 22nd AIAA/CEAS Aeroacoustics Conf., American Institute of Aeronautics and Astronautics, Reston, Virginia, 2016. doi:10.2514/6.2016-2873.
- [9] D.T. Blackstock, *Fundamentals of physical acoustics*, A WILEY-INTERSCIENCE, 2000.
- [10] T. Carolus, M. Schneider, H. Reese, Axial flow fan broad-band noise and prediction, *J. Sound Vib.* 300 (2007) 50–70. doi:10.1016/j.jsv.2006.07.025.
- [11] G. Leishman, *Principles of helicopter aerodynamics*, Cambridge University Press, 2006.
- [12] H. Hu, T. Wei, Z. Wang, An Experimental Study on the Wake Characteristics of Dual-Rotor Wind Turbines by Using a Stereoscopic PIV Technique, 34th AIAA Appl. Aerodyn. Conf. (2016). <http://arc.aiaa.org/doi/pdf/10.2514/6.2016-3128> (accessed April 6, 2017).